

Probing the interaction mechanism of heterostructured VOxNy nanoparticles supported in nitrogen-doped reduced graphene oxide aerogel as an efficient polysulfide electrocatalyst

*Original*

Probing the interaction mechanism of heterostructured VOxNy nanoparticles supported in nitrogen-doped reduced graphene oxide aerogel as an efficient polysulfide electrocatalyst for stable sulfur cathodes / Zubair, U.; Bianco, S.; Amici, J.; Francia, C.; Bodoardo, S.. - In: JOURNAL OF POWER SOURCES. - ISSN 0378-7753. - 461:(2020), p. 228144. [10.1016/j.jpowsour.2020.228144]

*Availability:*

This version is available at: 11583/2836581 since: 2020-06-19T12:52:38Z

*Publisher:*

Elsevier B.V.

*Published*

DOI:10.1016/j.jpowsour.2020.228144

*Terms of use:*

This article is made available under terms and conditions as specified in the corresponding bibliographic description in the repository

*Publisher copyright*

Elsevier postprint/Author's Accepted Manuscript

© 2020. This manuscript version is made available under the CC-BY-NC-ND 4.0 license  
<http://creativecommons.org/licenses/by-nc-nd/4.0/>. The final authenticated version is available online at:  
<http://dx.doi.org/10.1016/j.jpowsour.2020.228144>

(Article begins on next page)

# **Probing the interaction mechanism of heterostructured VO<sub>x</sub>N<sub>y</sub> nanoparticles supported in nitrogen-doped reduced graphene oxide aerogel as an efficient polysulfide electrocatalyst for stable Sulfur cathodes**

*Usman Zubair\**, Stefano Bianco, Julia Amici, Carlotta Francia, Silvia Bodoardo\*

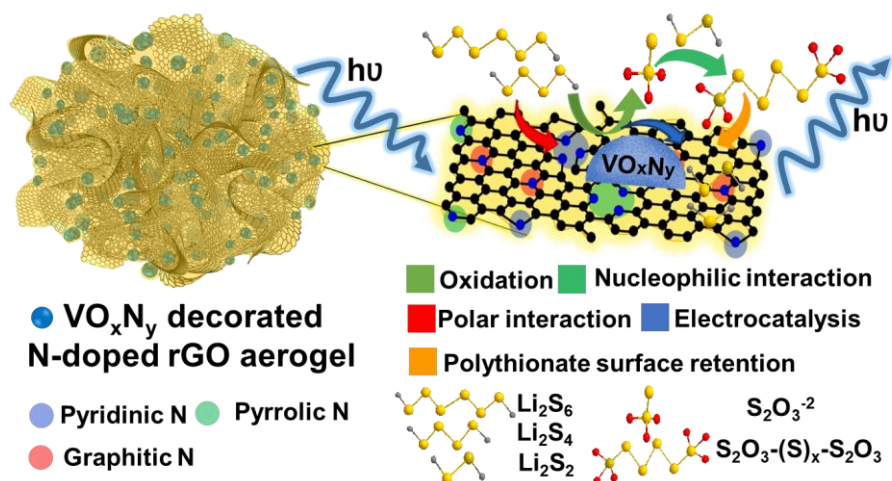
*Department of Applied Science and Technology, (DISAT), Politecnico di Torino, C.so Duca degli Abruzzi 24 - 10129 Torino – (ITALY).*

*\*Corresponding author. Tel.: +39 011 090 4641; fax: +39 011 090 4699. E-mail addresses: usman.zubair@polito.it; silvia.bodoardo@polito.it*

## **Abstract**

Reversible redox of sulfur to lithium sulfide through a series of lithium polysulfides (LiPS) still pose a key challenge to appreciate high-performance sulfur cathodes mainly because of their shuttling phenomenon and sluggish kinetics. It is hypothesized that transition metal compounds can be tuned to augment the interactions among oxides and LiPS by forming surface bound active redox intermediates. Herein, we exhibit a simple and novel synthetic approach to realize porous vanadium nitride oxide (VO<sub>x</sub>N<sub>y</sub>) nanoparticles spatially decorated within nitrogen doped reduced graphene aerogel (VONNG) via concurrent in-situ nitridation and carbonization processes. Nitrogen-doped reduced graphene aerogel offers a greater opportunity to enhance the physical retention and polar interaction of LiPS and contributes toward the overall conductivity of the matrix. Whereas, vanadium nitride oxide nanoparticles have exhibited a redox potential window intermediate to its oxides' counterparts around which LiPS can form polythionate complexes to enhance the kinetics and LiPS retention by exploiting the V-N and V-O interfaces at cathode. The interaction mechanism among LiPS and VO<sub>x</sub>N<sub>y</sub> has been probed through in-operando Raman spectroscopy, XPS and electroanalytical methods. The assembled cells from VONNG/S cathodes exhibit the initial discharge capacity of 1400 mAh g<sup>-1</sup> at 0.05 C, 1250 mAh g<sup>-1</sup> at 0.1 C and maintained their reversible capacity to 690 mA h g<sup>-1</sup> at 0.2 C for more than 200 cycles. The loss in capacity is recorded less than 0.03% per cycle for 850 cycles with Coulombic efficiency close to 99% even at 1 C.

## Graphical Abstract:



Vanadium nitride oxide ( $\text{VO}_x\text{N}_y$ ) nanoparticles have been realized in nitrogen doped reduced graphene oxide aerogel as an effective host matrix for efficient sulfur cathode. Probing the interaction mechanism between host material and polysulfides by XPS, in-operando Raman spectroscopy and electroanalytic tools has revealed that interface between V-O and V-N linkages can offer stronger binding interaction and fast electrocatalytical conversion of polysulfides.

**Keywords:** Vanadium nitride oxide, Lithium Sulfur, Polysulfides interaction, catalyst, In-operando Raman spectroscopy

## 1. Introduction

The lithium-sulfur (Li-S) batteries offer a promising solution to the ever-growing energy storage requests especially for electric mobility and grid storage in comparison to conventional Li-ion battery technologies<sup>1</sup>. This is mainly because of the high theoretical specific capacity (i.e. 1675 mAh g<sup>-1</sup>), high theoretical energy values (i.e. 2600 Wh kg<sup>-1</sup> or 2800 Wh L<sup>-1</sup>), environmental benignity and low cost of elemental sulfur<sup>2-4</sup>. Although, sulfur turns out as a prospective and sustainable answer in future energy conservation mix because of aforesaid characteristics, yet low sulfur utilization, fast capacity decay, poor Coulombic efficiency, short cycle life and serious self-discharge severely impede the practical deployment of Li-S batteries<sup>1,3</sup>. These impediments of Li-

S are essentially due to poor conductivity of terminal products  $S_8$  ( $5 \times 10^{-30} \text{ S cm}^{-1}$ ) and  $Li_2S$  ( $10^{15} \text{ S cm}^{-1}$ ), dissolution and shuttling of lithium polysulfides (LiPS), sluggish kinetics and morphological disruption of host matrix<sup>1,5</sup>. These long chain and short chain LiPS appear in two distinctive discharge plateaus about 2.3 V and 2.1 V, respectively. Numerous strategies have been implemented to realize efficient and stable sulfur cathodes. Different carbon matrices<sup>6</sup> have been investigated to host sulfur. Non-polar carbon surfaces cannot chemically interact with LiPS to immobilize sulfur species; instead, they rely on physical hosting of sulfur and its species. Contrary, elemental doped carbons<sup>7</sup> impart bond polarity to interact with LiPS to chemically engage LiPS within the cathode<sup>8</sup>.

Moreover, inorganic compounds described as sulfiphilic frameworks also offer greater polar surfaces to chemically interact with LiPS to restrict their dissolution into electrolyte<sup>9</sup>. However, merely physically trapping or polar interaction is not enough to alleviate LiPS shuttling and relieve sluggish kinetics. These two fundamental problems can be sorted out by catalysing the LiPS conversion into insoluble  $Li_2S_2$  and  $Li_2S$ . In the recent investigations, many nanostructured inorganic polar compounds such as metal oxides<sup>9,10</sup>, metal nitrides<sup>11,12</sup>, metal sulphides<sup>13,14</sup>, metal carbides<sup>15,16</sup> along with some metal-free substances<sup>17,18</sup> have been reported. Those compounds can curtail LiPS shuttle not only by offering a strong polar affinity towards LiPS but also by promoting catalytic conversion of LiPS to  $Li_2S_2/Li_2S$ <sup>19</sup>. Metal compounds can interact with LiPS via chemisorption or can exhibit acid base interactions and/or form a surface-bound active redox mediators<sup>20</sup>. Various hypotheses have been put forth to elaborate their electrocatalytic conversion mechanism and contribution towards alleviating LiPS shuttle<sup>21</sup>. One of such elucidation came up with idea of Goldilocks principle that highlights the exploitation of redox potential of transition metal oxides to oxidize LiPS into thiosulfate ( $S_2O_3^{2-}$ ) groups that in turn catenate with long chain LiPS to create surface bound polythionate complexes<sup>10</sup>. Nazar et al. also proposed the conversion of long chain LiPS into  $Li_2S$  through disproportionation reactions when electrically in contact with  $MnO_2$  surfaces in addition to suggested binding mechanism<sup>20</sup>. They have further proposed that transition metal oxides can be tuned to fall in Goldilock voltage window. One of such studies involves the study of  $VO_2$  and  $V_2O_5$  as hosting matrices for sulfur cathode<sup>10</sup>.

Metal sulfides exhibit higher conductivity than that of metal oxides, even carry metallic and half metallic phases<sup>19,22</sup>. Pang *et al.*<sup>13</sup> exhibited a metallic cobalt sulfide  $Co_9S_8$  as a host material

with a graphene-like interconnecting nanosheet architecture. The cathodes assembled using  $\text{Co}_9\text{S}_8$  showed excellent electrochemical performance with an initial discharge capacity of  $890 \text{ mAh g}^{-1}$  and a fading rate of  $0.045\%$  per cycle over 1500 cycles at  $C/2$ . This performance is delegated to metallic conductivity ( $290 \text{ S cm}^{-1}$ ) due to the existence of peritectic phase in the Co–S phase diagram, and hierarchical porosity of 3D structured  $\text{Co}_9\text{S}_8$  nanosheets that imparts superior absorptivity for LiPS. The anchoring of LiPS was confirmed studying the binding energy on  $\text{Co}_9\text{S}_8$  surfaces via a combination of first-principles calculations and XPS studies<sup>13</sup>.  $\text{MoS}_{2-x}/\text{rGO}$  has also been investigated with promising electrochemical performance. It has been demonstrated that sulfur deficient sites greatly contribute towards LiPS conversion and catalyze LiPS conversion kinetics. Because of higher participation in reaction chemistry, a very low quantity of  $\text{MoS}_{2-x}/\text{rGO}$  has a greater influence on electrochemical performance<sup>14</sup>. MXenes are the stacks of 2D transition metal carbides and carbonitrides. These 2D structures are intrinsically highly conductive and bear the chemically active surfaces to interact with polysulfides by metal-sulfur interaction. Nazar *et al.*<sup>15</sup> demonstrated MXene phase  $\text{Ti}_2\text{C}$  with 70 wt.% sulfur loading as an effective host for Li/S batteries without high surface area and well-ordered pores structure as required by other host materials. It is reported that sulfur and its lithium species are strongly held at metallic sites of highly conductive MXene phase  $\text{Ti}_2\text{C}$ .  $\text{S}/\text{Ti}_2\text{C}$  composite cathodes show excellent cycling performance with specific capacity  $1200 \text{ mAh/g}$  at  $C/5$  and capacity retention of 80% is achieved over 400 cycles at  $C/2$  current rate because of the strong interaction of the polysulfide species with the surface Ti atoms.

In recent years, transition metal nitrides and oxynitrides have also been intensively investigated as electrode or catalyst materials for several energy conversion and storage devices owing to the unique physical and chemical characteristics such as high conductivity, good electrochemical stability and high electrocatalytic activity like noble metal catalysts such as Pt<sup>23</sup>. More interest has been shown in the development of vanadium nitrides and oxynitrides composites as advanced electrode materials by the nitridation of various vanadium oxides precursors<sup>11</sup>. Both VN and  $\text{VO}_x\text{N}_y$  have been widely studied as pseudocapacitive electrode materials<sup>24,25</sup> because of fast faradic reactions as well as non-precious metal catalysts<sup>23</sup>. There are few reports in which TiN and VN have been investigated to host sulfur to realize remarkably stable cathodes<sup>12,26,27</sup>. Sun *et al.*<sup>27</sup> have proposed that VN has very high affinity and strong chemical adsorption capability for LiPS, and demonstrated that the binding energy among LiPS and VN ( $3.75 \text{ eV}$ ) is much higher than that of

usual carbon based materials (1.07 eV) through density functional theory calculations. In another report, the porous VN nanobelt arrays have been investigated, which offer a significant chemical interaction with LiPS arising from their high polar surface to restrain their shuttling towards the anode. It has been illustrated that porous VN nanobelt arrays can strongly absorb LiPS onto their surfaces due to strong polar-polar interactions among them to prevent the loss of active materials. Additionally, they have postulated that VN being electrocatalytically active also greatly contributes towards the accelerated electrochemical reaction kinetics<sup>28</sup>. Few reports have also explored heterostructure transition metal oxides and nitrides in combination for smooth immobilization-diffusion-conversion of LiPS. Yang *et al.*<sup>29</sup> has proposed a twinborn TiO<sub>2</sub>-TiN heterostructure electrode that enables a smooth trapping-diffusion-conversion of LiPS across the interface by taking the advantage of high absorptivity of TiO<sub>2</sub> and conductivity of TiN. In an alternative study, Fan *et al.*<sup>30</sup> reposted a VO<sub>2</sub>(B)-VN binary host, achieving smooth immobilization-diffusion-conversion of LiPS to enhance the electrochemical performance of Li-S batteries.

Hence, high performance sulfur cathodes can be appreciated by structuring novel multifunctional composites/hybrids by fabricating nanostructured elements into porous conductive matrices. This strategy allows the composite materials to come up with novel characteristics superior to those of individual components owing to synergistic performance of functional units. Moreover, the induction of porous nanostructures and high surface area support can also promote their electrochemical behaviours due to the improved conductivity of the composite and number of available active sites<sup>23,31</sup>. As discussed, vanadium oxide<sup>10,32</sup> and vanadium nitrides<sup>27,28</sup> are among the inorganic moieties that can interact with LiPS to extend the cycle life of Li/S cells. Thus, to induce the characteristics of both VO<sub>x</sub> and VN, instead of binary host<sup>30</sup>, carefully structured vanadium nitride oxide can enable to realize strong binding and electrocatalytical conversion of LiPS simultaneously to achieve a better host material. Herein, a novel and hassle-free approach is proposed to obtain vanadium oxynitride in nitrogen doped reduced graphene oxide rGO aerogel (VONNG) using commercial V<sub>2</sub>O<sub>5</sub> powder as a precursor. To acquire VO<sub>x</sub>N<sub>y</sub> decorated into carbon matrices, simultaneous in-situ ammonization and carbonization have been pursued. For the purpose, commercial V<sub>2</sub>O<sub>5</sub> powder has been mixed with hydrogen peroxide (H<sub>2</sub>O<sub>2</sub>) solution followed by mixing of graphene oxide solution to attain a hydrogel. The gel was dried and reduced under argon at 700 °C to achieve xerogel. This mixture was blended with

dicyanamide to carry out in-situ ammonization at 550 °C under nitrogen due to intermittent release of reactive nitrogen species followed by carbonization at 800 °C. As a result, a micro-structured hetero-interface VO<sub>x</sub>N<sub>y</sub> into N-doped rGO aerogel has been realized that can effectively suppress LiPS shuttle and enhance LiPS conversion kinetics. The VONNG/S cathodes show long term stability (850 cycles at with higher than 70% retention) at high current rate (1C). Additionally, the LiPS conversion mechanism and basis of faster redox kinetics have been investigated with various tools to underline the superiority of VO<sub>x</sub>N<sub>y</sub>.

## 2. Experimental Methods

### 2.1. Synthesis of Vanadium oxynitride (VO<sub>x</sub>N<sub>y</sub>) decorated Nitrogen-doped rGO

0.5 g of vanadium pentoxide (V<sub>2</sub>O<sub>5</sub>, Sigma Aldrich) was dispersed in 5 mL deionized water (DI, 18 MΩ at 25 °C). The mixture was added to 25 mL graphene oxide aqueous dispersion (4 mg/mL, Graphenea) to attain homogeneous mixture. 20 ml of H<sub>2</sub>O<sub>2</sub> solution (50 % v/v, Sigma Aldrich) was introduced in V<sub>2</sub>O<sub>5</sub>/GO mixture dropwise at 0 °C under vigorous stirring. The reaction was carried out for 6 h upholding the temperature around 0 °C to achieve a hydrogel. This ensures the separation of V<sub>2</sub>O<sub>5</sub> sheets and insertion of GO sheets among them. On reacting with H<sub>2</sub>O<sub>2</sub>, V<sub>2</sub>O<sub>5</sub> turns into hydrogen diperoxodioxovanadate (III) H<sub>3</sub>[VO<sub>2</sub>(O<sub>2</sub>)<sub>2</sub>]. The hydrogel was dried out at 90 °C to obtain xerogel weighing 0.68 g. The increase in weight than the sum of individual weights of precursors points to the occurrence of the reaction. As-obtained xerogel was subjected to reduction at 700 °C for 1 h under 3% H<sub>2</sub>/Ar gas mixture with heating rate 5 °C/min. On reduction, the mixture weight was reduced to 0.467 g that corresponds to the conversion of GO to rGO and reduction of H<sub>3</sub>[VO<sub>2</sub>(O<sub>2</sub>)<sub>2</sub>] to VO<sub>x</sub>.

Then, 5 g of dicyandiamide (Sigma Aldrich) was dissolved in 25 ml DI water under continuous stirring and heating, then 0.233 g of the as-synthesized reduced mixture was added to the solution. The dried grey coloured mixture was attained by heating mixture at 90 °C. The grey mass was heated first at 550 °C at a heating rate of 2.5 °C/min for 1 h under nitrogen flux. Then, the temperature was raised to 800 °C at 1 °C/min for 2 h to get a black aerogel. The weight of the obtained composite was around 0.255 g. The reaction involves in-situ ammonization and carbonization. The heating of dicyandiamide to 550 °C involves a solid condensation reaction to C<sub>3</sub>N<sub>4</sub> with the intermittent release of ammonia. Further, raise in temperature causes the synergetic release of nascent nitrogen species from C<sub>3</sub>N<sub>4</sub> and reduction of VO<sub>x</sub> to realize VO<sub>x</sub>N<sub>y</sub> decorated

N-doped rGO aerogel composite. The as-synthesized  $\text{VO}_x\text{N}_y/\text{N-doped rGO}$  aerogel composite is labelled as VONNG.

## **2.2. Construction of sulfur infiltrated VONNG and KJBC composite and cathodes**

Sulfur infiltrated VONNG composite was prepared in a weight ratio of 70:30. For the purpose, 140 mg of sulfur was dissolved into 1 mL of  $\text{CS}_2$ . Then, 60 mg of VONNG composite was added into the solution and the mixture was stirred to homogenize it. The mixture was dried under ambient condition and mortared for further homogenization. This mixture was transferred to heat furnace to achieve the melt infused composite. The mixture was heated at  $155\text{ }^\circ\text{C}$  for 6 h at heating rate  $1\text{ }^\circ\text{C}/\text{min}$  under argon flow. The final weight of sulfur-infused VONNG composite was around 180 mg and identified as VONNG/S. For electrodes, the slurry was prepared by mixing 80% VONNG/S, 10% carbon black (TIMICAL Super C45) and 10% polyvinylidene fluoride (PVDF) in N-methyl-2-pyrrolidone (NMP) using mixer mill (MM400, Retsch) at 20 Hz for 30 min. 15 mm discs were cut out for coin cell assembling and dried at  $50\text{ }^\circ\text{C}$  for 4 h under vacuum. The sulfur loading was around  $1.5\text{-}1.8\text{ mg cm}^{-2}$ .

## **2.3. Materials Characterization**

The morphology of VONNG and VONNG/S composites was examined using field-emission scanning electron microscopy (FESEM, JEOL-JSM-6700F). Energy dispersive X-ray spectroscopy (EDS) of the composites was also performed using JEOL-JSM-6700F. Elemental mapping is acquired under FESEM by imaging the X-ray signals from composite surface. Transmission electron microscopy analysis of VONNG aerogel was carried out using a JEOL JEM-2100 TEM. The XRD patterns were recorded on a Panalytical X'Pert PRO diffractometer with a PIXcel detector, using  $\text{Cu K}\alpha$  radiation, under the conditions of  $2\theta = 10\text{-}90^\circ$  and  $2\theta$  step size = 0.03, to observe the crystalline structures of  $\text{VO}_x/\text{rGO}$  and VONNG. X-ray photoelectron spectroscopy (XPS) analysis of VONNG and LiPS interacted VONNG were carried out using a Physical Electronics PHI5800 (USA) multi-technique ESCA system, with a monochromatic  $\text{Al K}\alpha$  X-ray radiation. For testing, the samples were placed in an ultrahigh vacuum chamber at  $2\times 10^{-10}$  Torr. Thermogravimetric analysis of VONNG/S was performed on a Mettler Toledo TGA/SDTA 851 instrument by heating the composite at  $10\text{ }^\circ\text{C min}^{-1}$  from room temperature to  $800\text{ }^\circ\text{C}$ . Raman spectroscopy of VONNG, and VONNG/S cathode was carried out on Renishaw

InVia micro-Raman spectrometer, with a laser excitation wavelength 785 nm and a laser spot size of  $\sim 20 \mu\text{m}$ .

#### **2.4. LiPS adsorption assessment, Li<sub>2</sub>S nucleation test, and In-operando Raman spectroscopy of VONNG/S cells**

For LiPS adsorption test, the solid Li<sub>2</sub>S<sub>6</sub> was prepared by mixing S<sub>8</sub> and Li<sub>2</sub>S with molar ratio of 5:1. Firstly, solution was prepared in an appropriate amount of tetrahydrofuran (THF) by mixing and heating at 50 °C under vigorous magnetic stirring for 48 h and, then evaporated of solvent. The 8 mg solid Li<sub>2</sub>S<sub>6</sub> was dissolved in 20 ml DME: DIOX mixture with 1/1 volume ratio. Then, solution divided into two parts; one is kept as a control, and in second 10 mg of VONNG aerogel has been introduced. The mixture was agitated and observed for visual color change after 1 h and 24 h. For Li<sub>2</sub>S precipitation test, similarly prepared solid Li<sub>2</sub>S<sub>8</sub> was dissolved in tetraglyme to realize 200 mM solution. The carbon paper (CP, SGL) and 1 mg VONNG loaded carbon paper (CP-VONNG) were soaked with 20  $\mu\text{L}$  Li<sub>2</sub>S<sub>8</sub>/tetraglyme solution and used as 12 mm electrodes for test. EH2010 separator and Li were saturated with 20  $\mu\text{L}$  1 M LiTFSI/tetraglyme solution and used in assembling the coin cell. Li<sub>2</sub>S nucleation and growth tests were performed by first galvanostatically discharging the cell to 2.06 V at 0.112 mA and then potentiostatically discharging under 2.05 V until the current was below  $10^{-5}$  A. Then, current profiles were evaluated by Faraday's law to estimate the quantity Li<sub>2</sub>S precipitation. For in-operando analysis, in house assembled pouch cells with borosilicate glass window have been used. The cells were assembled as per configuration highlighted in the scheme (Fig. 6a). The cathode surface has been directly probed to observe the real time on sight conversion of various sulfur redox species. The cells were subjected to a rational current rate of 0.1C. The spectra were acquired after every 20 min with 2 data acquisition of 60 sec. The spectra were baselined and used as it is to infer equitably.

#### **2.5. Electrochemical measurements**

The coin cells 2032 were assembled using as-prepared cathodes versus metallic lithium anode with EH2010 (trilayer PP/PE/PP) separator with electrolyte to sulfur (E/S) ratio  $< 10 \mu\text{L mg}^{-1}$  of sulfur. Coin cells 2032 were assembled in Ar-filled dry glove box (Mbraun Labstar with O<sub>2</sub> and H<sub>2</sub>O  $< 0.1$  ppm). The geometric area of the electrodes was 1.76 cm<sup>2</sup>. A lithium disc (16 x 0.2 mm, Chemetall s.r.l.) was used as anode. A Celgard EH2010 20 mm x 20  $\mu\text{m}$  was soaked with the electrolyte composed of 1,2-dimethoxyethane (DME) and 1,3-dioxolane (DIOX) 1:1 (v/v) with 1

M lithium bis(trifluoromethanesulfonyl)imide ( $\text{CF}_3\text{SO}_2\text{NLiSO}_2\text{CF}_3$ , LiTFSI) and 0.25 M lithium nitrate ( $\text{LiNO}_3$ ). Cells were galvanostatically discharged to 1.8 V and charged to 2.6 V vs.  $\text{Li/Li}^+$  by an Arbin BT-2000 battery tester at room temperature. Cycling tests were performed at various C-rate. The C-Rate is calculated using the theoretical capacity of sulfur (i.e.)  $1672 \text{ mA h g}^{-1}$ . Cyclic voltammetry (CV) and electrochemical impedance spectroscopy (EIS) measurements were performed on CH instrument electrochemical workstation using three electrodes configuration using  $\text{Li/Li}^+$  as reference and counter electrodes. CV of VONNG/S cathode was carried out between 1.5 and 3 V at  $0.01 \text{ mV sec}^{-1}$ , while CV of VONNG was performed vs. Li between 1.6 and 3.4 V. Electrochemical impedance spectra (EIS) were measured from 1 Hz to 100 kHz with a potential amplitude of 10 mV.

### 3. Results and Discussion

The steps involved in the synthesis of vanadium nitride oxide nanoparticles spatially distributed in nitrogen doped graphene aerogel (VONNG) are schematically illustrated in Fig. 1. This strategy allows one-shot production of host material for sulfur cathode exploiting the ease of hydrogel synthesis and advantage of concurrent in-situ nitridation and carbonization processes to offer onsite ammonia reactor. For the purpose, vanadium pentoxide ( $\text{V}_2\text{O}_5$ ) is dispersed into graphene oxide dispersion followed by addition of  $\text{H}_2\text{O}_2$  (50%) to realize a dark brownish hydrogel at low temperature. The reaction of vanadium(V) oxide with  $\text{H}_2\text{O}_2$  come up with hydrogen diperoxodioxovanadate(III) ( $\text{H}_3[\text{VO}_2(\text{O}_2)_2]$ ) by following reaction.



The hydrogel was subjected to  $700 \text{ }^\circ\text{C}$  under 3%  $\text{H}_2/\text{Ar}$  to achieve a xerogel with partially reduced graphene oxide and vanadium (III) oxide ( $\text{V}_2\text{O}_3$ ). This conversion has been probed by performing XRD analysis of as obtained  $\text{V}_x\text{O}_y/\text{rGO}$  xerogel. Fig. 4a depicts a hump around  $26^\circ$  that represents rGO in the matrix, while the XRD peak pattern exactly coincides to Karelianite structure ( $\text{V}_2\text{O}_3$ ). The  $\text{VO}_x/\text{rGO}$  xerogel was mixed and homogenized with dicyanamide before subjecting to two step heat treatment under nitrogen environment. In the first step, the mixture was exposed to  $550 \text{ }^\circ\text{C}$  to carry out the thermal condensation of dicyanamide to carbon nitride ( $\text{C}_3\text{N}_4$ ) with abundant release of ammonia<sup>33</sup>. On further raising the temperature to  $800 \text{ }^\circ\text{C}$ , the carbon nitride carbonized to defected graphene structure with further release of ammonia and active nitrogen species, while occurring the transformation of partial reduced graphene oxide into nitrogen doped graphene

aerogel. The in-situ release of ammonia and active nitrogen gaseous species enable the conversion of vanadium (III) oxide into  $\text{VO}_x\text{N}_y$ <sup>34</sup>, conversion of rGO into nitrogen doped graphene, and formation of the finest aerogel structure. The presence of graphene oxide and  $\text{C}_3\text{N}_4$  among the particles restrict the boundary growth of nanoparticles and assist to realize the porous structure of  $\text{VO}_x\text{N}_y$ , that ensure maximum interface to exploit electrocatalytical activity as a host material in sulfur cathode.

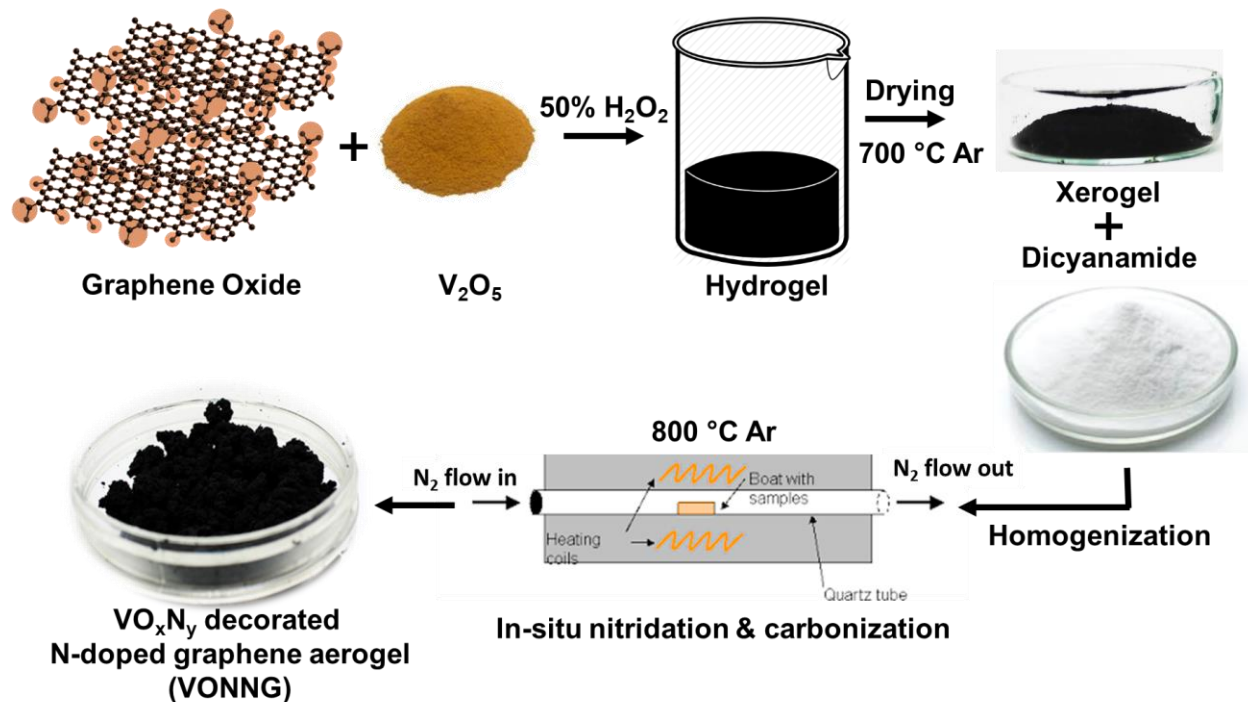


**Figure 1.** Schematic illustration of the synthesis strategy opted to produce VONNG aerogel.

### 3.1. Characterization of spatially manufactured multifunctional VONNG aerogel and its sulfur composite

Morphological characterization of VONNG and VONNG/S composites has been visualized by FESEM and HRTEM. The as-prepared VONNG composite exhibited an architecture that comprised of several nanoscale porous  $\text{VO}_x\text{N}_y$  particles incorporated inside 3D nitrogen doped rGO fine aerogel network fostered by rGO sheets (Fig. 2, 3). However, some buildups of  $\text{VO}_x\text{N}_y$  can be observed due to aggregation but HRTEM reveals that boundary growth of nanoparticles has been confined owing to the presence of carbon structures (Fig. 3). This restricted growth phenomenon results in realization of porous assemblies of  $\text{VO}_x\text{N}_y$  nanoparticles. Fig. 2b and c reveals highly porous architecture of nitrogen doped rGO aerogel. Fig. 2a shows the backscatter

FESEM imaging of VONNG aerogel to spot the  $\text{VO}_x\text{N}_y$  nanoparticles (marked orange) just exist in a few top layers of rGO. VONNG/S composite also exhibits a similar morphology with a stuffing effect that is due to the melt infusion of sulfur into the structure of VONNG aerogel (Fig. 2d, e). The element mapping spectrum of VONNG to demonstrate the distribution of  $\text{VO}_x\text{N}_y$  nanoparticles in the composites (Fig. 2f). It could be inferred from V, N and O mapping that  $\text{VO}_x\text{N}_y$  are uniformly distributed across the aerogel. Fig. S1 represents the EDS spectrum of selected area of the composite with inset table representing the wt.% value of C, V, N and O. On taking the line EDS spectrum across the buildup of nanoparticles (Fig. S2), the strength of the N and O signal along with V substantiates the existence of vanadium nitride oxide ( $\text{VO}_x\text{N}_y$ ) particles.

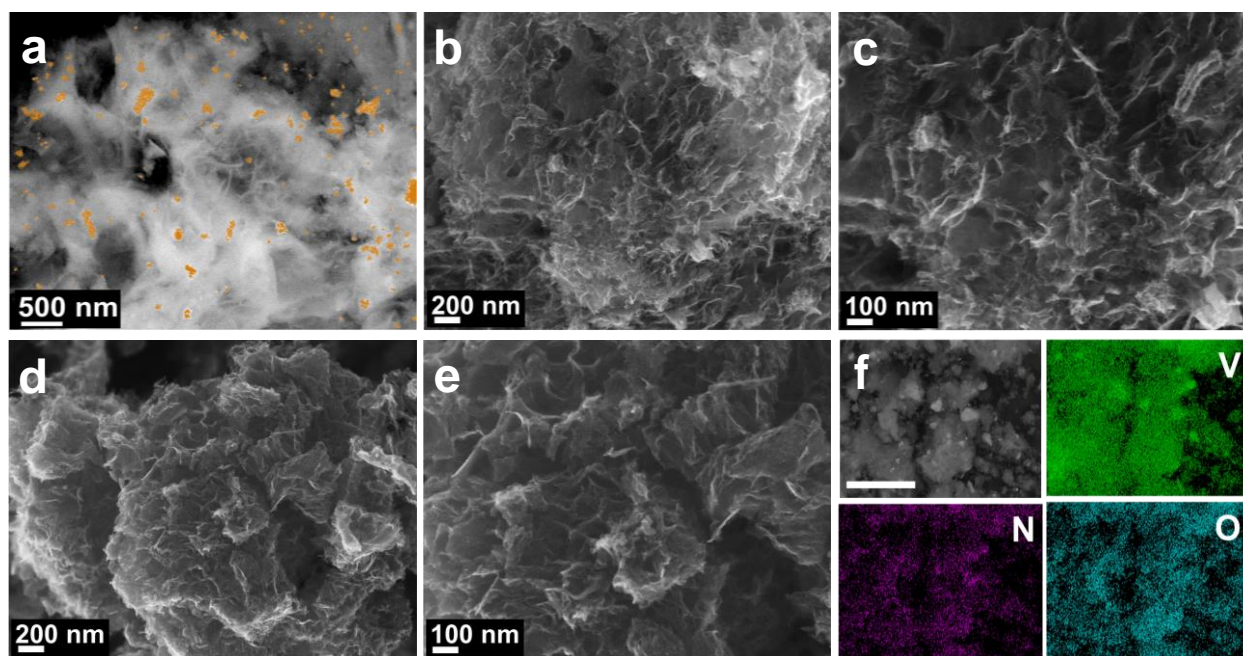


**Figure 2:** (a) Back scattered imaging of VONNG aerogel highlighting the  $\text{VO}_x\text{N}_y$  nanoparticles existing just underneath few layers of rGO aerogel. FESEM images of (b,c) VONNG matrix. (d,e) sulfur-infused VONNG composite; f) EDS mapping of the VONNG composite (scale bar 2  $\mu\text{m}$ ).

Fig. 3 illustrates the morphological elements of VONNG aerogel by high-resolution TEM (HRTEM). It can be observed that porous nanoparticles ranging in the dimension of 10-50 nm have been spatially distributed into the rGO aerogel owing to topotactic transformation<sup>35</sup>.  $\text{VO}_x\text{N}_y$  nanoparticles are enveloped by interconnected network of nitrogen doped rGO sheets. The HRTEM imaging exhibits the lattice fringes with interfringe spacing of 0.209 nm, which corresponds to the d-spacing of 200 planes of cubic  $\text{VO}_x\text{N}_y$  (Fig. 3c). On performing the Fourier transformation of the Fig. 3c (insert), other planes (111, 220 and 311) related to cubic  $\text{VO}_x\text{N}_y$

structure can be resolved because of principal transformation of the  $\text{VO}_x$  particles. This fact has been corroborated by XRD and XPS analyses too. As for VONNG composite,  $\text{VO}_x\text{N}_y$  nanoparticles with a few tens of nanometers in diameter are uniformly wrapped and supported by network of well interpenetrated rGO sheets that appear more transparent to the electron beam.

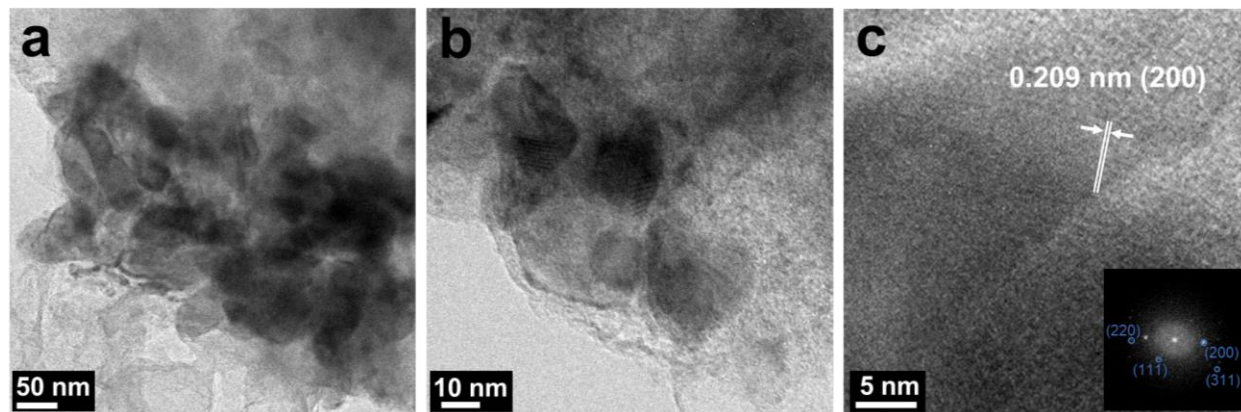


**Figure 3:** (a,b) HRTEM images of VONNG aerogel characterizing the presence of  $\text{VO}_x\text{N}_y$  nanoparticles at tenth order of nm in rGO aerogel. (c) HRTEM image of  $\text{VO}_x\text{N}_y$  particle pointing the inter fringe distance of 0.209 nm (inset) the FFT of the image indicating plane of cubic  $\text{VO}_x\text{N}_y$ .

XRD analysis of as-obtained  $\text{VO}_x/\text{rGO}$  intermediate xerogel and VONNG aerogel were performed to outline the crystalline structure of the composites (Fig. 4a, b). Intermediate  $\text{VO}_x/\text{rGO}$  composite displayed a typical pattern of  $\text{V}_2\text{O}_3$  on rGO. The peak pattern exactly complements with JCPDS index 34-0187 that represents Karelitanite ( $\text{V}_2\text{O}_3$ ) structure (Fig. 4a). The hump around  $26^\circ$  can be clearly observed that characterizes rGO in the composite. The XRD pattern of VONNG as shown in Fig. 4b exhibited typical five diffraction peaks ranging from  $35^\circ$  to  $85^\circ$  that are related to cubic  $\text{VO}_x\text{N}_y$  structure on JCPDS index 00-037-1178/9<sup>35</sup>. The five observed peaks that also matches well with (111), (200), (220), (311) and (222) planes of the typical stoichiometric face-centered (fcc) VO (JCPDS No. 75-0048) or VN (JCPDS No. 73-0528) structures<sup>23,24</sup>. The XRD confirmed the presence of fcc cubic  $\text{VO}_x\text{N}_y$  in composite without any residual peak from vanadium oxide precursor, which confirms the complete in-situ nitridation of  $\text{VO}_x$  precursor. The realization of  $\text{VO}_x\text{N}_y$  compound can be ascribed to less harsh and absence of wholesome ammonia ( $\text{NH}_3$ ) environment to carry out complete transformation of oxide into nitride. Additionally, a broad peak for VONNG composite appears at about  $26^\circ$  that is related to the (002) plane of graphite carbon (JCPDS No. 75-1261) and confirms the presence of rGO sheets.

The Raman spectrum has been carried out to examine graphitic structure of nitrogen doped rGO aerogel and to observe the Raman signature of  $\text{VO}_x\text{N}_y$ . The Raman bands at 273, 444, 514, 697.5, and 997  $\text{cm}^{-1}$  can be assigned to the typical modes of vanadium oxide<sup>32</sup> with a small shift owing to the presence of nitrogen in the structure<sup>36</sup>. Additionally, some new peaks can be spotted peculiar to the  $\text{VO}_x\text{N}_y$  structure<sup>28</sup>. The dominance of Raman response by vanadium oxide can be attributed to presence of more oxygen in the outer layers due to air oxidation. As formed high oxygen rich  $\text{VO}_x\text{N}_y$  is minor in the structure and present on the surface, so it is too small to be detected by XRD (Fig. 4b). However, XPS analysis, (Fig. 4 d, e) being a surface analysis technique, can come up even with more compelling signals from vanadium oxide. Moreover, Raman spectroscopy of rGO aerogel has provided two carbon characteristic Lorentzian peaks, one is around 1358  $\text{cm}^{-1}$  disorder “D” band and other is around 1590  $\text{cm}^{-1}$  graphitic “G” band (Fig. 4c). The ID/IG ratio of the rGO aerogel was estimated by fitting the spectra with Lorentz function to assess the degree of graphitization<sup>37</sup>. ID/IG value average around 0.7 characterizing high degree of graphitization as anticipated, hence offer higher conductivity.

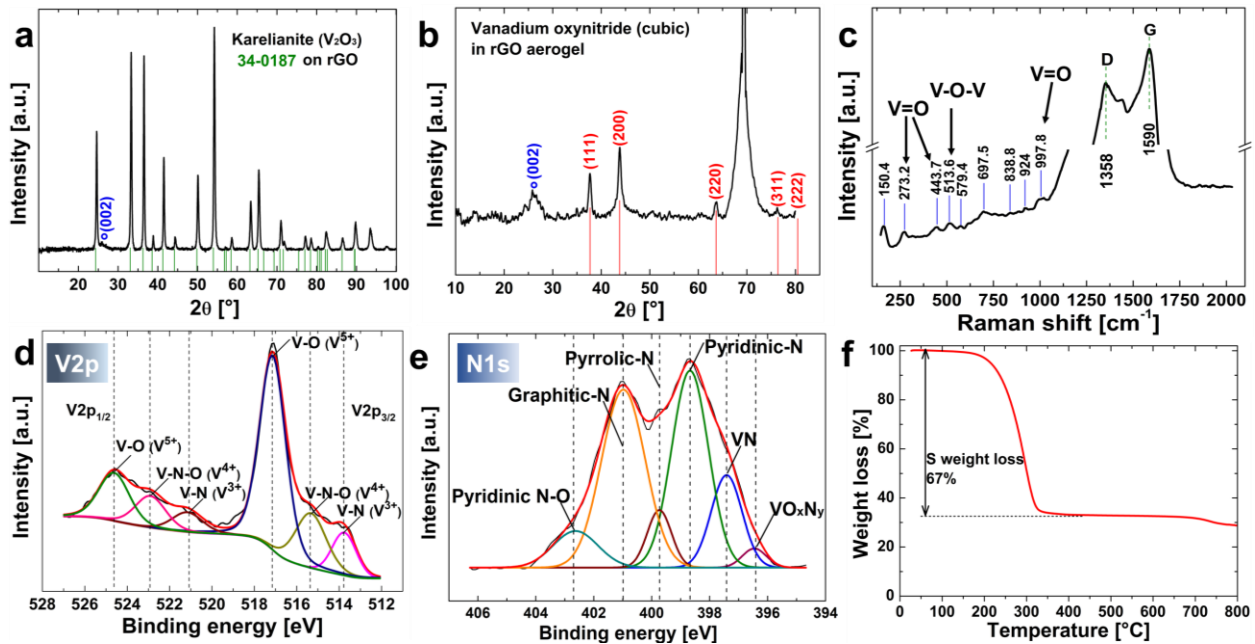


**Figure 4:** XRD spectra of (a) intermediate  $\text{VO}_x/\text{rGO}$  complex, (b) VONNG aerogel underlining the presence of cubic vanadium oxynitride. (c) Raman spectrum of VONNG composite exhibiting V-O modes at various Raman shifts owing to nitrogen presence. XPS of VONNG aerogel (d) V2p spectrum (e) N1s spectrum indicating presence of organic and inorganic nitrogen linkages.

To understand the electronic and atomic environment, high resolution XPS analysis has been performed. XPS survey spectra of VONNG signals the presence of vanadium (V), nitrogen (N), oxygen (O), and carbon (C) elements (Fig. S3a). A 2p doublet can be observed for vanadium in the binding energy range between 512 to 528 eV with three distinctive peaks of  $V^{3+}$ ,  $V^{4+}$ , and  $V^{5+}$  for V-N, V-N-O, and V-O respectively (Fig. 4d). Peaks around 514 eV ( $2p_{3/2}$ ) and 521 eV ( $2p_{1/2}$ ) can be assigned to V bonded to N in the crystal lattice. While, other four peaks at 515.4 eV ( $2p_{3/2}$ ), 523 eV ( $2p_{1/2}$ ), and 517.1 eV ( $2p_{3/2}$ ), 524.8 eV ( $2p_{1/2}$ ) can be designated to vanadium nitride oxide and vanadium oxide in  $VO_xN_y$  respectively<sup>23,25,36</sup>. There is a shakeup satellite peak around 519 eV that is arising from the surface oxygen O1s in the  $VO_xN_y$  lattice<sup>38</sup>. As previously emphasized that air aging and surface adsorption of hydroxyl oxygen at  $VO_xN_y$  particles would result in more oxygen rich outer layers, this is the most probable reason of having intense signals of vanadium oxide. Fig. 4e depicts the chemical environment of N in VONNG aerogel. The peaks in N1s can be resolved in two distinguished zones; one is related to metal nitride and oxynitride while other N peaks related to bonding with C in nitrogen doped rGO aerogel. The two peaks of N1s spectra at 397.5 eV and 396.4 eV correspond to metal nitride (V-N) and metal oxynitride (V-N-O) bonding of  $VO_xN_y$  nanoparticles present in the matrix<sup>39</sup>. While peaks at about 398.8 eV, 399.85 eV, and 401 eV are linked to pyridinic, pyrrolic and graphitic bonded nitrogen to graphene matrices as illustrated in the scheme Fig. 7. The peak at 402.8 eV corresponds to pyridinic N-O<sup>40</sup>. High resolution C1s spectra of VONNG (Fig. S3b) exhibits the binding energy band at 284.8 eV that corresponds to adventitious carbon (C-C, C=C) and marked as a reference to shift the spectra. In addition, surface bonded oxygen species come up with peaks at about 285.2 eV, 287.9 eV, and 290 eV, those are related to C-OH, C=O, and COOH groups respectively. The C1s spectrum also exhibited a peak at 286.5 eV that is related to the typical C-N-C group in a graphitic carbon nitride framework<sup>41</sup>. These results specify that rGO aerogel in VONNG aerogel is functionalized with N and O atoms that impart polarity to the matrix for a strong chemical interaction with LiPS. TGA analysis of VONNG/S composite was performed under argon atmosphere to estimate the sulfur in the composite. VONNG/S exhibited a mass loss around 67 wt. % at 300 °C that corresponds to evaporation of sulfur (Fig. 4f). The loss in mass is equivalent to the mass of sulfur in the composite. A loss in mass can be witnessed about 700 °C that can be ascribed to further reduction and nitridation of  $VO_xN_y$  particles and decomposition of nitrogen doped carbon structures.

### 3.2. LiPS adsorption and electrocatalytic interaction through visual assessment test, XPS, Li<sub>2</sub>S precipitation test, In-operando Raman spectroscopic analysis, and cyclic voltammetry

To probe the interaction mechanism of VO<sub>x</sub>N<sub>y</sub> with LiPS, a visualized adsorption assessment test of VONNG was carried out using 20mM stock solution of Li<sub>2</sub>S<sub>6</sub> in DME: DIOX 1:1 (V/V) mixture in Argon filled glove box. 10 mg of VONNG aerogel was introduced into the as prepared Li<sub>2</sub>S<sub>6</sub> solution. VONNG matrix enabled to decolorize the Li<sub>2</sub>S<sub>6</sub> solution within an hour by resting the mixture after a strong shake up (Fig. 5a). On resting the solution for 24 h, the VONNG decolorized the mixture nearly to transparent. To further elucidate the interaction chemistry, XPS analysis of the Li<sub>2</sub>S<sub>6</sub> adsorbed VONNG mixture was performed. For the purpose, the mixture was filtered and evaporated of solvents under stringent Argon environment and transferred to the XPS instrument. XPS spectra were resolved for the high resolution of V, S and O to underline the interaction mechanism. Fig. 5b reveals that for O1s, the Li<sub>2</sub>S<sub>6</sub> interacted VONNG showed an additional and strong signal at binding energy 531.62 eV that corresponds to O-S bonding in comparison to oxygen signal arising from VONNG matrix<sup>42</sup>. This additional peak highlights the conversion of LiPS into oxidized state sulfur species such as thiosulfate on encountering VO<sub>x</sub>N<sub>y</sub>. On observing the XPS spectrum of Li<sub>2</sub>S<sub>6</sub> interacted VONNG for V2p region, (Fig. 5c), two supplementary peaks can be traced at 515.25 eV in V2p<sub>3/2</sub> band and 521.33eV for V2p<sub>1/2</sub> that corresponds to V-S interaction binding energies or reduction of VO<sub>x</sub>N<sub>y</sub><sup>43-45</sup>. This emphasises the fact that first LiPS has strong binding interaction with vanadium of VO<sub>x</sub>N<sub>y</sub> porous nanoparticles. Secondly, the surface reduction of VON may associated to the oxidation of LiPS. So, it can be inferred that VO<sub>x</sub>N<sub>y</sub> can perform both chemical interaction and catalytical activation of LiPS. This fact further corroborated by witnessing the S2p XPS spectrum of the mixture (Fig. 5d). In addition to binding energy peaks correspond to terminal and bridging sulfur of LiPS<sup>20</sup>, peaks correspond to oxidized sulfur<sup>10</sup> and V-S interaction can be spotted<sup>43,46</sup>. Oxidized sulfur peaks around 168.2 eV confirm the formation of polythionate complexes to limit the LiPS solubility into electrolyte<sup>20</sup>. The catalytic conversion of LiPS into thiosulfate can be assisted by VO<sub>x</sub>N<sub>y</sub> that in turn complex with LiPS to form polythionates to restrain free LiPS solubility to electrolyte. V-S interaction peak appears about 159.88 eV that also highlighting the strong polar interaction between vanadium of VO<sub>x</sub>N<sub>y</sub> and sulfur of LiPS<sup>46</sup>.

From the cyclic voltammetry (CV) of VONNG (Fig. 9a), it can also be inferred that onset redox potential of  $\text{VO}_x\text{N}_y$  is around 2.8 V that is well above the 2.4 V related to LiPS conversion. The higher redox potential of  $\text{VO}_x\text{N}_y$  triggers the conversion of LiPS, those are in close vicinity, into oxide species such as thiosulfate<sup>10</sup>. This oxidation happens at the expense of the partial reduction of surface vanadium ( $\text{V}^{+5}$ ,  $\text{V}^{+4}$ ) species into  $\text{V}^{+4}$  and  $\text{V}^{+3}$ . The optimal redox potential of VON porous nanoparticles mostly instigates the mild oxidation of LiPS into thiosulfate, instead of irreversible and ineffective sulfate formation<sup>10</sup>. This fact can be observed on further resolving the oxidized sulfur peak into multicomponent. The XPS S2p contribution at 170.2 eV that corresponds to sulfate ( $\text{SO}_4^{2-}$ ) is minimal in comparison to thiosulfate ( $\text{S}_2\text{O}_3^{2-}$ ) at 167.2 eV. The redox contribution of  $\text{VO}_x\text{N}_y$  versus  $\text{Li}/\text{Li}^+$  is also nominal even during the initial CVs of VONNG/S cathode as demonstrated with arrows in the Fig. 9a.  $\text{Li}_2\text{S}$  nucleation and growth test marked as an effective strategy that features the fast conversion of LiPS to  $\text{Li}_2\text{S}$  to curtail the LiPS shuttle and to relieve the sluggish redox kinetics<sup>11,47</sup>. In summary,  $\text{Li}_2\text{S}$  precipitation reflects the suitability of the host matrix to augment the sulfur utilization and to improve the cycle life of the sulfur cathodes. Fig. 5e, f reports the  $\text{Li}_2\text{S}$  precipitation curve of CP and CP-VONNG, respectively. In the figures, dark shaded area corresponds to the capacity contributions coming from the reduction of long chain LiPS ( $\text{Li}_2\text{S}_8$  and  $\text{Li}_2\text{S}_6$ ). From the remaining light shaded areas, the capacities of  $\text{Li}_2\text{S}$  precipitation have been evaluated by the current integration according to Faraday's law. The capacity values estimated around 91.3  $\text{mAh g}^{-1}$  and 203  $\text{mAh g}^{-1}$  for CP and CP-VONNG, respectively that clearly suggests far improved  $\text{Li}_2\text{S}$  nucleation capability of VONNG matrix.

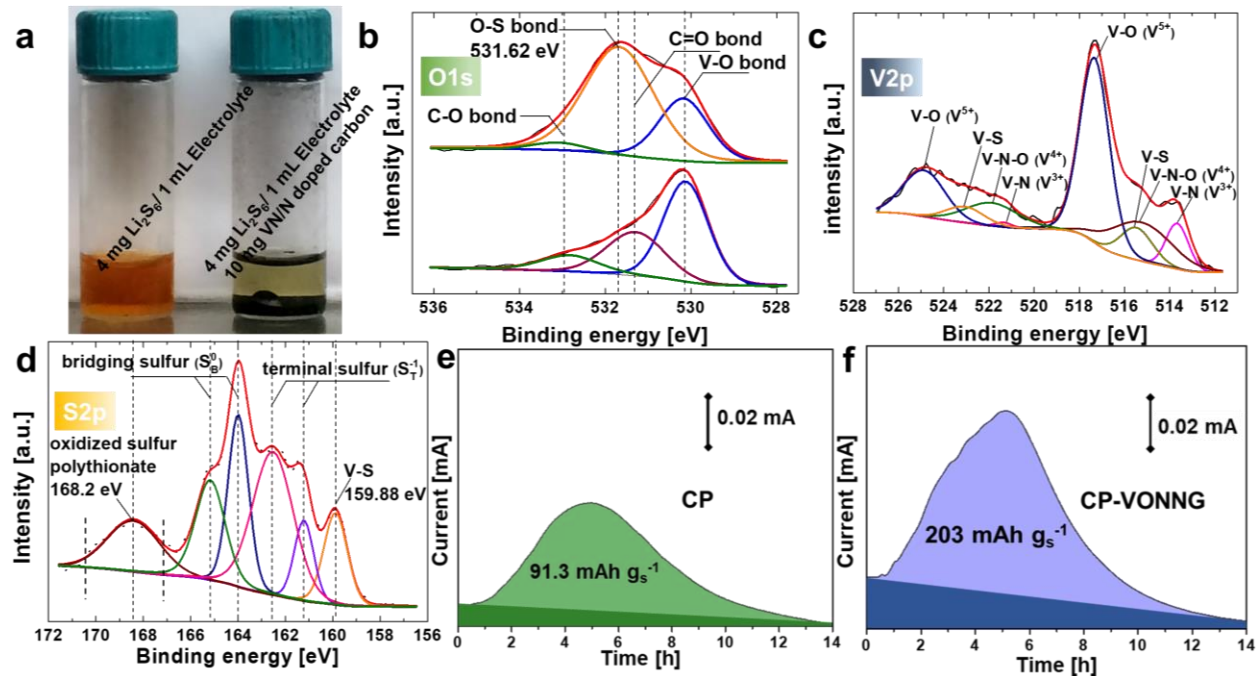
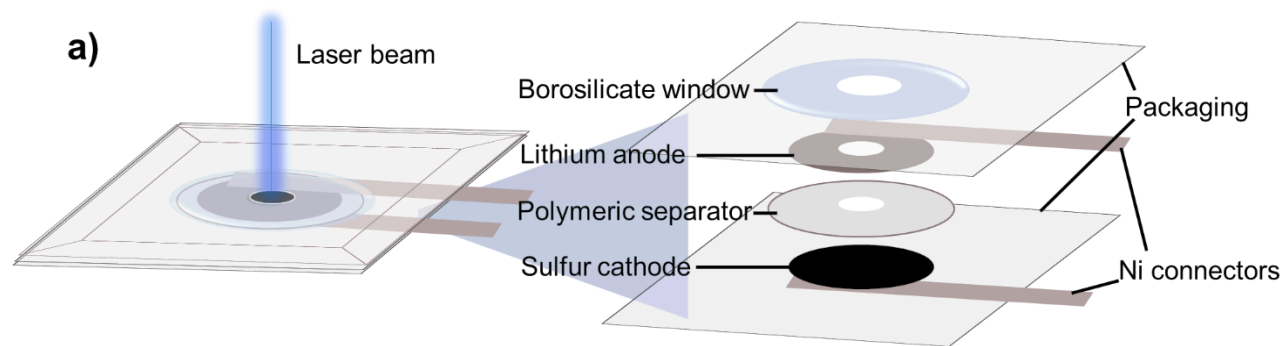


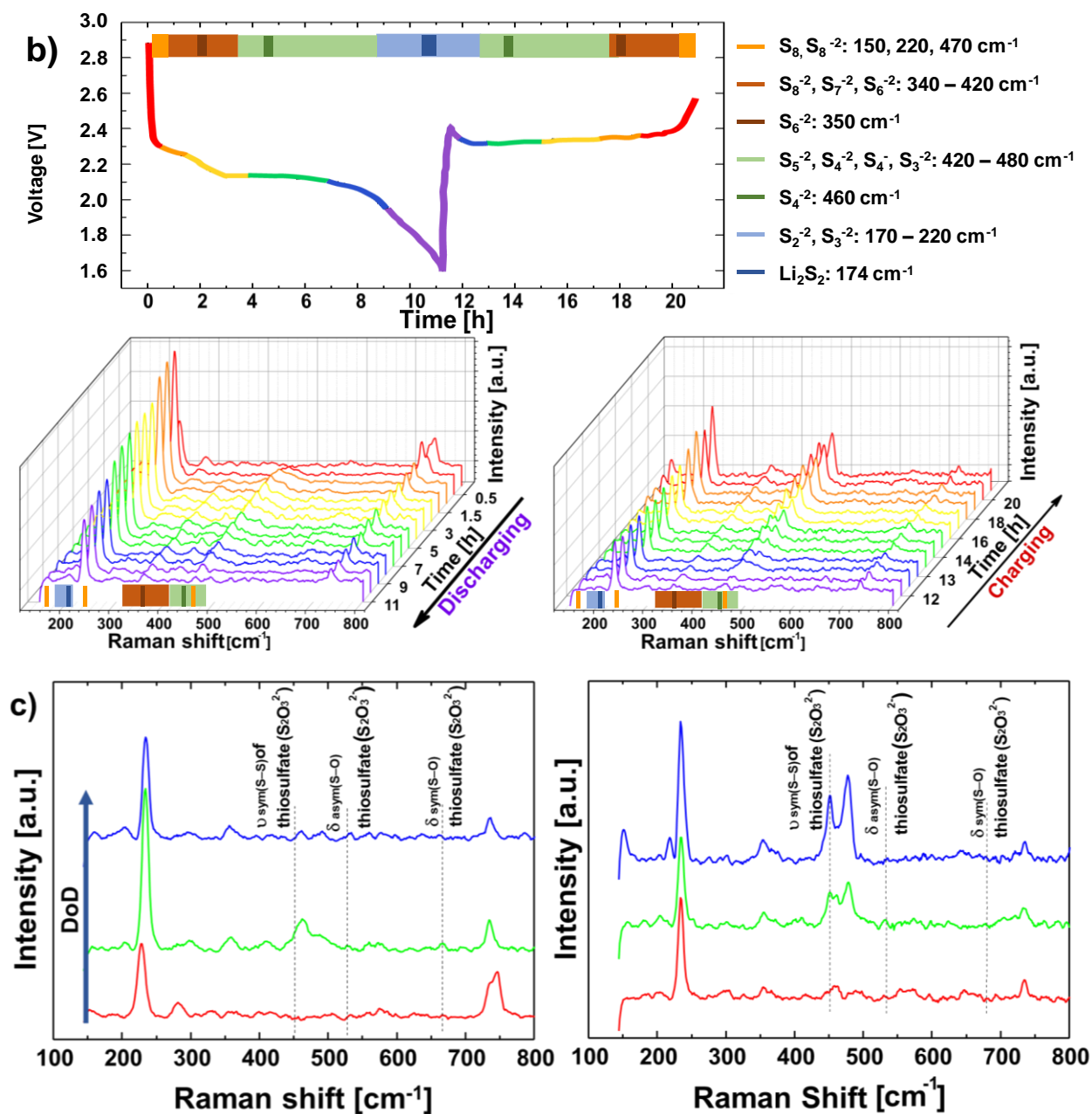
**Figure 5:** (a) Experimental demonstration of LiPS adsorption capability of VONNG composite (control vs 1 h exposed). XPS analysis of LiPS interacted VONNG matrix (b) O1s spectrum, VONNG (bottom) vs. absorbed (top) (c) V2p spectrum of interacted sample (d) S2p spectrum of interacted LiPS. Li<sub>2</sub>S nucleation test of Li<sub>2</sub>S<sub>8</sub>/tetraglyme solution (e) carbon paper (f) 1 mg loaded VONNG carbon paper.

In-operando Raman spectroscopy of VONNG/S cathode was performed in accordance to the configuration proposed in the scheme Fig. 6a. To enquire the interaction mechanism and LiPS evolution during the cell operation, the surface of cathode was irradiated with 782 nm laser to collect the Raman scattered response of the species appearing during charge and discharge. The assignment of the Raman peaks for elemental sulfur (S<sub>8</sub>), lithium polysulfides (LiPS) and oxidized sulfur species has been acquired from literature<sup>48-50</sup>. Table S1 presents the value of Raman shift of various LiPS. At open circuit potential, the VONNG/S cathode exhibited the peaks about 150 and 220 cm<sup>-1</sup> related to elemental S<sub>8</sub>. In early 30 min of discharge the peak around 220 cm<sup>-1</sup> intensified because of the appearance of S<sub>8</sub><sup>-2</sup> species into catholyte. This peak then gradually shortens on discharging the cathode, underlining the conversion of S<sub>8</sub><sup>-2</sup>. Meanwhile, the appearance of the peaks between 340-420 cm<sup>-1</sup> features the conversion of Li<sub>2</sub>S<sub>8</sub> into medium chain and short chain LiPS. Raman shift between 340 to 420 cm<sup>-1</sup> can be assigned to long chain LiPS such as S<sub>8</sub><sup>-2</sup>, S<sub>7</sub><sup>-2</sup> and S<sub>6</sub><sup>-2</sup>, while peaks of Raman shift between 420-480 cm<sup>-1</sup> can be designated to medium chain LiPS such as S<sub>4</sub><sup>-2</sup>, S<sub>4</sub><sup>-</sup> and S<sub>3</sub><sup>-2</sup>. After 2 h of discharge, S<sub>4</sub><sup>-2</sup> appears around 460 cm<sup>-1</sup> that disappears on last 2 hour of discharge. The 460 cm<sup>-1</sup> peak climax on 5 hours of discharge as

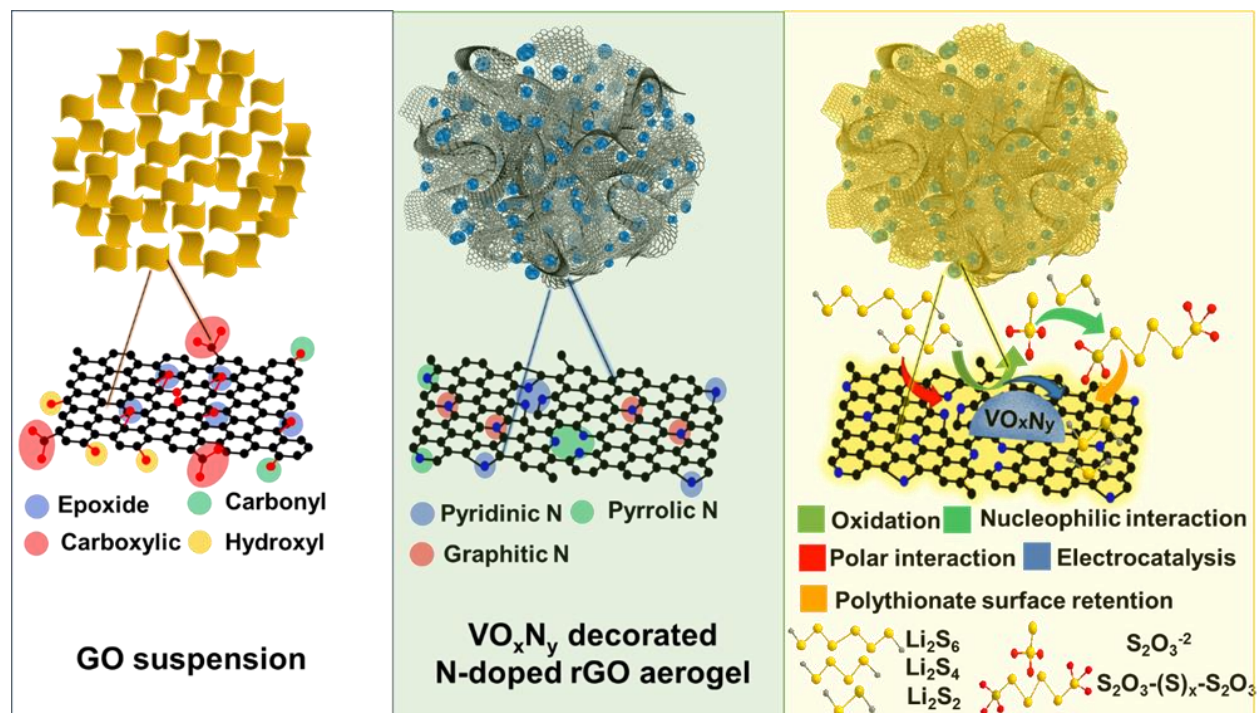
highlighted in Fig. 6b. The disappearance of  $\text{Li}_2\text{S}_4$  corresponds to the appearance of peaks around  $170\text{-}220\text{ cm}^{-1}$  related to  $\text{S}_3^{2-}$  and  $\text{S}_2^{2-}$  species. Particularly, the peak about  $174\text{ cm}^{-1}$  becomes visible at the end of discharge linked to the Raman shift of  $\text{Li}_2\text{S}_2$ . Contrary, on charging  $\text{Li}_2\text{S}_2$  peak disappears in initial couple of hours of charging followed by the emergence of peaks between  $340\text{-}480\text{ cm}^{-1}$ . The peak around  $460\text{ cm}^{-1}$  got intensified on increment the state of charge (SoC). Further, increase in SoC results in growth of  $350\text{ cm}^{-1}$  peak related to  $\text{S}_6^{2-}$ . At 100% SoC, the peaks around  $150$ ,  $220$  and  $470\text{ cm}^{-1}$  emerged and intensified, demonstrating the shift of  $\text{Li}_2\text{S}_2$  into  $\text{S}_8^{2-}$  and ultimately to elemental sulfur  $\text{S}_8$ .

Fig. 6c illustrates the electrocatalytical conversion of LiPS into thiosulfate ( $\text{S}_2\text{O}_3^{2-}$ ) that ultimately form polythionate complexes with LiPS. Presence of thiosulfate species can be detected by closely observing Raman spectra at various depth of discharge (DoD) and SoC during the cell operation. Various Raman responses of thiosulfate has been recorded, and the assignment of peaks is opted from the literature<sup>51,52</sup>. The band around  $450\text{ cm}^{-1}$  corresponds to the stretching vibrations of thiosulfate. The bands around  $530$  and  $680\text{ cm}^{-1}$  can be respectively assigned to asymmetric and symmetric stretching vibration of thiosulfate. It can be observed that initially there is no band related to thiosulfate at OCV just after assembling the cell. On subsequent discharging, the thiosulfate band reduced to a least after an initial growth because of their ultimate reduction to  $\text{Li}_2\text{S}$ . On charging, unlithiated  $\text{VOxNy}$  particles are reclaimed, meanwhile thiosulfate bands kept on growing again owing to surface reoxidation of LiPS on incrementing the SoC as per previous reports<sup>10,20</sup>. The phenomena stated here can be traced back to CV again. This underlines first time that electrocatalytical formation of thiosulfate can also be observed during cell operation along with reversible redox of  $\text{S}_8$  to  $\text{Li}_2\text{S}$ .





**Figure 6:** (a) Schematic sketch of the pouch cell configuration with quartz glass window used for in-operando Raman study of VONNG/S cathode. (b) Galvanostatic discharge and charge profile and corresponding development of in-operando Raman spectra collected at the surface of VONNG/S cathode at a regulated interval during discharge and charge labelled with growth of various LiPS. (c) In-operando Raman spectra of thiosulfates appears during cell operation at various DoD and SoC



**Figure 7.** Schematic sketching of the study that outlines from material synthesis to interaction mechanism of VONNG aerogel as a prospective host material for sulfur cathodes.

### 3.3. Stable electrochemical performance of VONNG/S cathodes

As prepared VONNG/S cathodes were evaluated for their electrochemical performance using lithium anode. The VONNG/S cells were subjected to galvanostatic charging and discharging at various C-rates. Each cell was subjected to specific current equivalent to 0.1C for the first two cycles between 1.8 and 2.6 V, and then subsequent long cycling was carried out between 1.8 and 2.6 V at various C-rates to investigate the stability of as prepared VONNG/S cathodes. It can be observed that for the first cycle at 0.1C, VONNG/S cathode has delivered the specific capacity around 1300 mAh g<sup>-1</sup> in both cases as depicted in Fig. 8a. Then, one cell that has been cycled at 0.2C, showed the first cycle capacity about 1013 mAh g<sup>-1</sup>. Even after 200 cycles, the capacity retention was 64 % that is 690 mAh g<sup>-1</sup>. In the second case, when the cell was subjected to 0.5C C-rate, the first cycle capacity was 814 mAh g<sup>-1</sup>. On further cycling, the retained capacity was 560 mAh g<sup>-1</sup> after 200 cycles that is 62% of initial capacity at 0.5C. Moreover, at 0.5C, the capacity retention was about 54% of initial capacity even after 500 cycles of charging and discharging with Coulombic efficiency of 98.5% (Fig. S4).

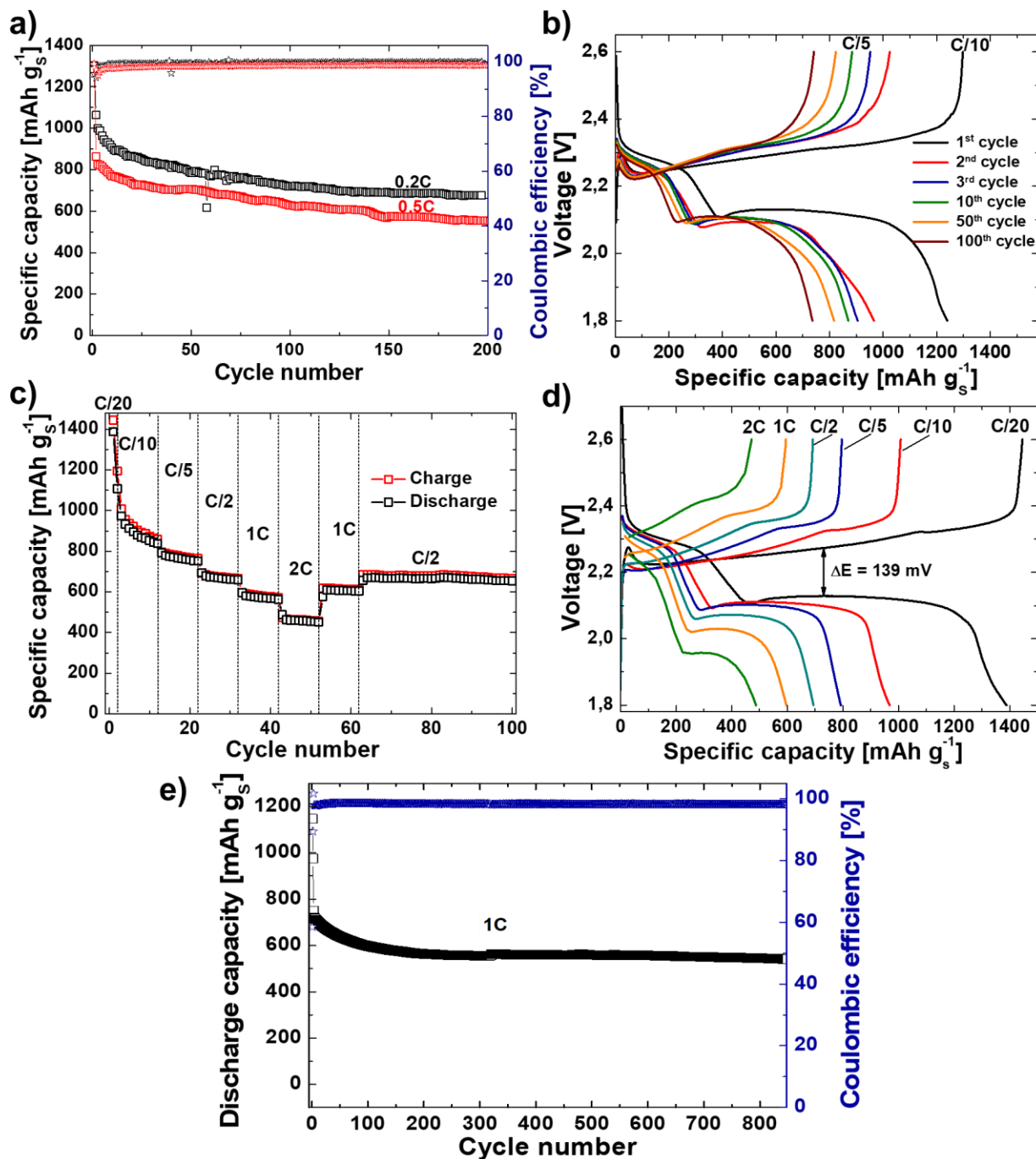


**Figure 8:** (a) Cycling performance of VONNG/S composite electrodes at specific currents corresponds to 0.2C and 0.5C with Coulombic efficiencies. (b) Corresponding discharge-charge profiles at 0.2C up to 200 cycles. (c) Rate response of the VONNG/S composite at various C-rate from 0.05C to 2C. (d) Corresponding discharge-charge profiles for each C-rate test. and (e) Long term cycling behavior at a high C-rate of 1 C for 850 cycles with Coulombic efficiency.

From the voltage profile, typical behavior of sulfur cathodes can be depicted (Fig 8 b,d). There exist two distinct plateaus at 2.3 and 2.1 V for discharging curves, while during charge the

major plateau appears at 2.4 V. The existence of typical plateaus points out the conductivity (low polarizability) and suitability of the chosen morphology or architecture. Moreover, the potential gap  $\Delta E$  (difference of overpotential of charge and discharge plateaus) can be recorded about 139 mV at 0.05C and 0.1C (Fig. 8c), hence the hysteresis of discharging and charging minimized that also points out kinetic enhancement of sulfur cathodes. To further evaluate the rate capability performance of the VONNG/S cathode, the cells were exposed to various C-rates ranging from 0.05C to 2C. The values of specific capacity have been recorded approximately as 1400 mAh g<sup>-1</sup> at 0.05C, 1050 mAh g<sup>-1</sup> at 0.1C, 793 mAh g<sup>-1</sup> at 0.2C, 694 mAh g<sup>-1</sup> at 0.5C, 608 mAh g<sup>-1</sup> at 1C and 496 mAh g<sup>-1</sup> at 2C (Fig. 8d). The cell exhibited appreciable recovery when subjected back to lower C-rate after 10 cycles charging and discharging at 2C as shown in the Fig. 8c. This indicates the material responsiveness in term of its capability to function as an efficient host material for sulfur and LiPS. A little polarization can be observed as a little increase in overpotential at higher C-rates (2C). This behavior is comprehensible when the insulating sulfur loading is about 70 wt.% of the matrix. However, even at 2C cathode material continued to exhibit the typical plateaus, but the polarization posed by the composite becomes a little pronounced that underlines kinetic sustainability of VONNG matrix. The long cycle life stability analysis was performed at 1C, VONNG/S cathode initially exhibited a capacity of about 740 mAh g<sup>-1</sup> with a capacity retention of 70% after 850 cycles (Fig 8e). Such a capacity retention at high specific current points out the matrix capability to improve the sulfur redox kinetics and to lessen the shuttling effect.

To further examine VONNG/S cathodes' electrochemical behavior, cyclic voltammetry (CV) and electrochemical impedance spectroscopy (EIS) have been performed. Three CV cycles have been carried out between 1.5 and 3 V at 0.01 mV sec<sup>-1</sup>. During sweep from 3 to 1.5 V, two sulfur reduction peaks can be observed at 2.23 and 1.9 V. One peak at 1.9 V is a broader with a little shoulder around 2V, but for two subsequent cycles this peak shifts 2 V and becomes symmetric. This inconsistent behavior can be attributed to irreversible redox of VONNG matrix and buildup of SEI layer formation. While during the sweep from 1.5 to 3 V, a strong oxidation peak pivot around 2.45 V with a strong shoulder peak around 2.6-2.7 V. This shoulder also narrows down for the next two cycles around 2.6 V (Fig. 9a). CV of VONNG matrix points out some contributions in CV of VONNG/S coming from lithiation and delithiation of VO<sub>x</sub>N<sub>y</sub> particles. Although these contributions are great for first cycle but for subsequent cycles these influences become nominal. Consistency among the CVs of 2nd and 3rd cycles also demonstrate the

stabilization of the system. This exactly corresponds to first cycle Galvanostatic charging-discharging where VONNG/S cathode always exhibits a much greater capacity value than that of succeeding cycles. EIS measurements were also accomplished before and after cycling (Fig. 9b). The diameter of the semicircle at low frequencies characterizing the charge-transfer resistance ( $R_{ct}$ ) greatly decreases during cycling. Very small  $R_{ct}$  value signifies very high conductivity and strong affinity of VONNG matrix towards LiPS.

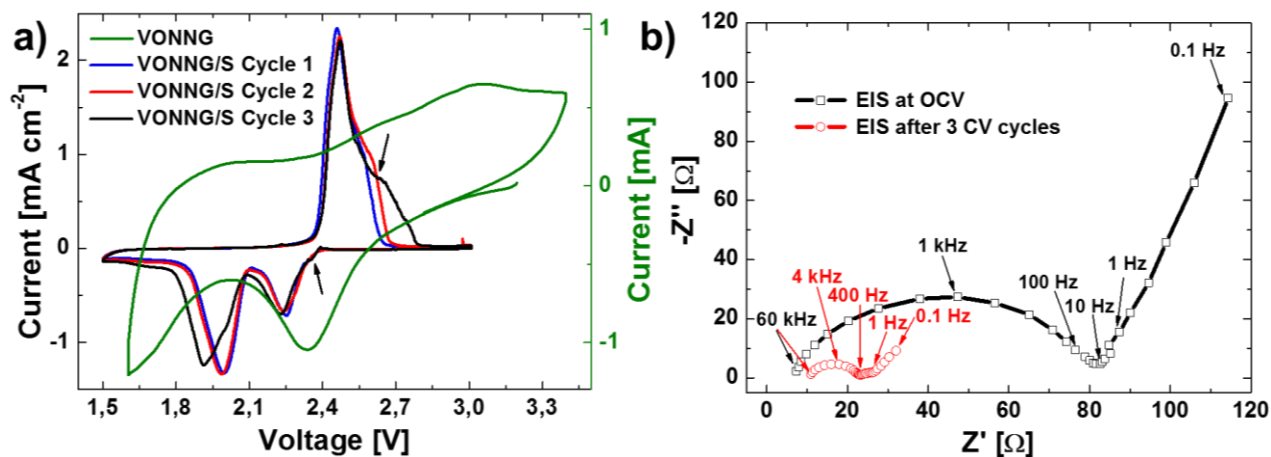


**Figure 9:** (a) Cyclic voltammetry of VONNG aerogel and VONNG/S cathode (first 3 cycles). CV of VONNG confirms a redox potential higher than that of 2.4 V, while CV of VONNG/S cathode even exhibits initial contribution from redox of VONNG at a slow scan rate. (b) Electrochemical impedance spectroscopy of VONNG/S cathode at OCV and after 3 cycles of CV.

#### 4. Conclusions

In summary, vanadium nitride oxide ( $VO_xN_y$ ) nanoparticles have been synthesized in nitrogen-doped rGO aerogel via in-situ ammonization and carbonization. VONNG exhibited a very strong interaction with the LiPS. Vanadium nitride offers a strong binding, fast electrons transfer and fast electrocatalytic activity, while vanadium oxides demonstrate a strong catalytic redox conversion towards LiPS. By fabricating heterostructured  $VO_xN_y$ , individual characteristics can be exploited at interface between V-O and V-N linkages to offer even stronger binding interaction and fast electrocatalytical conversion of LiPS.  $VO_xN_y$  also offers a redox potential window vs.  $Li/Li^+$  greater than that of 2.4 V of LiPS conversion to ensure the redox of LiPS to assist their retention at cathode. Nitrogen doped rGO aerogel also offer a polar interaction, conductivity and physical retention towards VONNG composite. Owing to these features, the assembled battery thus has a high specific capacity, high rate capability, higher Coulombic efficiency, and long cycling

performance. Moreover, a simple and effective strategy has been proposed as an effective solution to promote the practical use of Li/S batteries by catalytically suppressing the shuttling of LiPS.

## Acknowledgments

Financial support was provided by the European Union H2020 NMP-17-2014 ALISE (GA 666157).

## Appendix A. Supporting Information

Supplementary data related to the article can be found at DOI:

## Figure Captions

**Figure 1.** Schematic illustration of the synthesis strategy opted to produce VONNG aerogel.

**Figure 2:** (a) Back scattered imaging of VONNG aerogel highlighting the VO<sub>x</sub>Ny nanoparticles existing just underneath few layers of rGO aerogel. FESEM images of (b,c) VONNG matrix. (d,e) sulfur-infused VONNG composite; f) EDS mapping of the VONNG composite (scale bar 2 μm).

**Figure 3:** (a,b) HRTEM images of VONNG aerogel characterizing the presence of VO<sub>x</sub>Ny nanoparticles at tenth order of nm in rGO aerogel. (c) HRTEM image of VO<sub>x</sub>Ny particle pointing the inter fringe distance of 0.209 nm (inset) the FFT of the image indicating plane of cubic VO<sub>x</sub>Ny.

**Figure 4:** XRD spectra of (a) intermediate VO<sub>x</sub>/rGO complex, (b) VONNG aerogel underlining the presence of cubic vanadium oxynitride. (c) Raman spectrum of VONNG composite exhibiting V-O modes at various Raman shifts owing to nitrogen presence. XPS of VONNG aerogel (d) V2p spectrum (f) N1s spectrum indicating presence of organic and inorganic nitrogen linkages.

**Figure 5:** (a) Experimental demonstration of LiPS adsorption capability of VONNG composite (control vs 1 h exposed). XPS analysis of LiPS interacted VONNG matrix (b) O1s spectrum, VONNG (bottom) vs. absorbed (top) (c) V2p spectrum of interacted sample (d) S2p spectrum of interacted LiPS. Li<sub>2</sub>S nucleation test of Li<sub>2</sub>S<sub>8</sub>/tetraglyme solution (e) carbon paper (f) 1 mg loaded VONNG carbon paper.

**Figure 6:** (a) Schematic sketch of the pouch cell configuration with quartz glass window used for in-operando Raman study of VONNG/S cathode. (b) Galvanostatic discharge and charge profile and corresponding development of in-operando Raman spectra collected at the surface of VONNG/S cathode at a regulated interval during discharge and charge labelled with growth of various LiPS. (c) In-operando Raman spectra of thiosulfates appears during cell operation at various DoD and SoC.

**Figure 7:** Schematic sketching of the study that outlines from material synthesis to interaction mechanism of VONNG aerogel as a prospective host material for sulfur cathodes.

**Figure 8:** (a) Cycling performance of VONNG/S composite electrodes at specific currents corresponds to 0.2C and 0.5C with Coulombic efficiencies. (b) Corresponding discharge-charge profiles at 0.2C up to 200 cycles. (c) Rate response of the VONNG/S composite at various C-rate from 0.05C to 2C. (d) Corresponding discharge-charge profiles for each C-rate test. and (e) Long term cycling behavior at a high C-rate of 1 C for 850 cycles with Coulombic efficiency.

**Figure 9:** (a) Cyclic voltammetry of VONNG aerogel and VONNG/S cathode (first 3 cycles). CV of VONNG confirms a redox potential higher than that of 2.4 V, while CV of VONNG/S cathode even exhibits initial contribution from redox of VONNG at a slow scan rate. (b) Electrochemical impedance spectroscopy of VONNG/S cathode at OCV and after 3 cycles of CV.

## References

- 1 Seh, Z. W., Sun, Y., Zhang, Q. & Cui, Y. Designing high-energy lithium-sulfur batteries. *Chem Soc Rev* **45**, 5605-5634, doi:10.1039/c5cs00410a (2016).
- 2 Pope, M. A. & Aksay, I. A. Structural Design of Cathodes for Li-S Batteries. *Advanced Energy Materials* **5**, 1500124, doi:10.1002/aenm.201500124 (2015).
- 3 Caixia, L., Zhucong, X., Dexiang, G., Xiangju, C. & Longwei, Y. Chemical Immobilization Effect on Lithium Polysulfides for Lithium–Sulfur Batteries. *Small* **14**, 1701986, doi:doi:10.1002/sml.201701986 (2018).

- 4 Lacey, M. J. *et al.* A Robust, Water-Based, Functional Binder Framework for High-Energy Lithium-Sulfur Batteries. *ChemSusChem* **10**, 2758-2766, doi:10.1002/cssc.201700743 (2017).
- 5 Wild, M. *et al.* Lithium sulfur batteries, a mechanistic review. *Energy & Environmental Science* **8**, 3477-3494, doi:10.1039/C5EE01388G (2015).
- 6 Zhou, G. M. *et al.* A graphene foam electrode with high sulfur loading for flexible and high energy Li-S batteries. *Nano Energy* **11**, 356-365, doi:10.1016/j.nanoen.2014.11.025 (2015).
- 7 Yin, L.-C. *et al.* Understanding the interactions between lithium polysulfides and N-doped graphene using density functional theory calculations. *Nano Energy* **25**, 203-210, doi:<https://doi.org/10.1016/j.nanoen.2016.04.053> (2016).
- 8 Zubair, U., Amici, J., Crespiera, S. M., Francia, C. & Bodoardo, S. Rational design of porous carbon matrices to enable efficient lithiated silicon sulfur full cell. *Carbon* **145**, 100-111, doi:<https://doi.org/10.1016/j.carbon.2019.01.005> (2019).
- 9 Pang, Q., Kundu, D., Cuisinier, M. & Nazar, L. F. Surface-enhanced redox chemistry of polysulphides on a metallic and polar host for lithium-sulphur batteries. *Nat Commun* **5**, 4759, doi:10.1038/ncomms5759 (2014).
- 10 Liang, X. *et al.* Tuning Transition Metal Oxide-Sulfur Interactions for Long Life Lithium Sulfur Batteries: The "Goldilocks" Principle. *Advanced Energy Materials* **6**, doi:Artn 1501636 10.1002/Aenm.201501636 (2016).
- 11 Song, Y. *et al.* Enhanced Sulfur Redox and Polysulfide Regulation via Porous VN-Modified Separator for Li-S Batteries. *ACS Applied Materials & Interfaces* **11**, 5687-5694, doi:10.1021/acsami.8b22014 (2019).
- 12 Hao, Z. *et al.* TiN as a simple and efficient polysulfide immobilizer for lithium-sulfur batteries. *Journal of Materials Chemistry A* **4**, 17711-17717, doi:10.1039/C6TA07411A (2016).
- 13 Chen, T. *et al.* Metallic and polar Co<sub>9</sub>S<sub>8</sub> inlaid carbon hollow nanopolyhedra as efficient polysulfide mediator for lithium-sulfur batteries. *Nano Energy* **38**, 239-248, doi:<https://doi.org/10.1016/j.nanoen.2017.05.064> (2017).
- 14 Lin, H. *et al.* Electrocatalysis of polysulfide conversion by sulfur-deficient MoS<sub>2</sub> nanoflakes for lithium-sulfur batteries. *Energy & Environmental Science* **10**, 1476-1486, doi:10.1039/C7EE01047H (2017).

- 15 Liang, X., Garsuch, A. & Nazar, L. F. Sulfur cathodes based on conductive MXene nanosheets for high-performance lithium-sulfur batteries. *Angew Chem Int Ed Engl* **54**, 3907-3911, doi:10.1002/anie.201410174 (2015).
- 16 Peng, H. J. *et al.* Enhanced Electrochemical Kinetics on Conductive Polar Mediators for Lithium-Sulfur Batteries. *Angew Chem Int Ed Engl* **55**, 12990-12995, doi:10.1002/anie.201605676 (2016).
- 17 Meng, Z. *et al.* Graphene-like g-C<sub>3</sub>N<sub>4</sub> nanosheets/sulfur as cathode for lithium-sulfur battery. *Electrochimica Acta* **210**, 829-836, doi:<https://doi.org/10.1016/j.electacta.2016.06.032> (2016).
- 18 Li, L. *et al.* Phosphorene as a Polysulfide Immobilizer and Catalyst in High-Performance Lithium-Sulfur Batteries. *Adv Mater* **29**, doi:10.1002/adma.201602734 (2017).
- 19 Liu, X., Huang, J. Q., Zhang, Q. & Mai, L. Nanostructured Metal Oxides and Sulfides for Lithium-Sulfur Batteries. *Adv Mater* **29**, doi:10.1002/adma.201601759 (2017).
- 20 Liang, X. *et al.* A highly efficient polysulfide mediator for lithium-sulfur batteries. *Nat Commun* **6**, 5682, doi:10.1038/ncomms6682 (2015).
- 21 Liu, D. *et al.* Catalytic Effects in Lithium-Sulfur Batteries: Promoted Sulfur Transformation and Reduced Shuttle Effect. *Adv Sci (Weinh)* **5**, 1700270, doi:10.1002/advs.201700270 (2018).
- 22 Xiao, Z., Yang, Z., Zhou, L., Zhang, L. & Wang, R. Highly Conductive Porous Transition Metal Dichalcogenides via Water Steam Etching for High-Performance Lithium-Sulfur Batteries. *ACS Appl Mater Interfaces* **9**, 18845-18855, doi:10.1021/acsami.7b04232 (2017).
- 23 Huang, K. *et al.* Porous VO<sub>x</sub>Ny nanoribbons supported on CNTs as efficient and stable non-noble electrocatalysts for the oxygen reduction reaction. *Scientific Reports* **5**, 17385, doi:10.1038/srep17385 (2015).
- 24 Wang, R., Lang, J., Zhang, P., Lin, Z. & Yan, X. Fast and Large Lithium Storage in 3D Porous VN Nanowires-Graphene Composite as a Superior Anode Toward High-Performance Hybrid Supercapacitors. **25**, 2270-2278, doi:10.1002/adfm.201404472 (2015).
- 25 Shu, D. *et al.* Soft-template synthesis of vanadium oxynitride-carbon nanomaterials for supercapacitors. *International Journal of Hydrogen Energy* **39**, 16139-16150, doi:<https://doi.org/10.1016/j.ijhydene.2014.05.119> (2014).

- 26 Li, X. *et al.* Freestanding carbon encapsulated mesoporous vanadium nitride nanowires enable highly stable sulfur cathodes for lithium-sulfur batteries. *Nano Energy* **40**, 655-662, doi:<https://doi.org/10.1016/j.nanoen.2017.09.018> (2017).
- 27 Sun, Z. *et al.* Conductive porous vanadium nitride/graphene composite as chemical anchor of polysulfides for lithium-sulfur batteries. *Nat Commun* **8**, 14627, doi:10.1038/ncomms14627 (2017).
- 28 Zhong, Y. *et al.* Confining Sulfur in Integrated Composite Scaffold with Highly Porous Carbon Fibers/Vanadium Nitride Arrays for High-Performance Lithium–Sulfur Batteries. *Advanced Functional Materials* **28**, 1706391, doi:10.1002/adfm.201706391 (2018).
- 29 Zhou, T. *et al.* Twinborn TiO<sub>2</sub>–TiN heterostructures enabling smooth trapping–diffusion–conversion of polysulfides towards ultralong life lithium–sulfur batteries. *Energy & Environmental Science* **10**, 1694-1703, doi:10.1039/C7EE01430A (2017).
- 30 Song, Y. *et al.* Synchronous immobilization and conversion of polysulfides on a VO<sub>2</sub>–VN binary host targeting high sulfur load Li–S batteries. *Energy & Environmental Science* **11**, 2620-2630, doi:10.1039/C8EE01402G (2018).
- 31 Hao, B. *et al.* Reviving catalytic activity of nitrides by the doping of the inert surface layer to promote polysulfide conversion in lithium-sulfur batteries. *Nano Energy* **60**, 305-311, doi:<https://doi.org/10.1016/j.nanoen.2019.03.064> (2019).
- 32 Wang, S. *et al.* Designing a highly efficient polysulfide conversion catalyst with paramontroseite for high-performance and long-life lithium-sulfur batteries. *Nano Energy* **57**, 230-240, doi:<https://doi.org/10.1016/j.nanoen.2018.12.020> (2019).
- 33 Claridge, J. B., York, A. P. E., Brungs, A. J. & Green, M. L. H. Study of the Temperature-Programmed Reaction Synthesis of Early Transition Metal Carbide and Nitride Catalyst Materials from Oxide Precursors. *Chemistry of Materials* **12**, 132-142, doi:10.1021/cm9911060 (2000).
- 34 Yang, Y. *et al.* Novel Hybrid Nanoparticles of Vanadium Nitride/Porous Carbon as an Anode Material for Symmetrical Supercapacitor. **9**, 6, doi:10.1007/s40820-016-0105-5 (2016).
- 35 Panda, R. N. & Kaskel, S. J. J. o. M. S. Synthesis and characterization of high surface area molybdenum nitride. **41**, 2465-2470, doi:10.1007/s10853-006-5112-3 (2006).

- 36 Ghimbeu, C. M., Raymundo-Piñero, E., Fioux, P., Béguin, F. & Vix-Guterl, C. Vanadium nitride/carbon nanotube nanocomposites as electrodes for supercapacitors. *Journal of Materials Chemistry* **21**, 13268-13275, doi:10.1039/C1JM11014D (2011).
- 37 Ferrari, A. C. & Robertson, J. Interpretation of Raman spectra of disordered and amorphous carbon. *Physical Review B* **61**, 14095-14107, doi:10.1103/PhysRevB.61.14095 (2000).
- 38 Mendiáldua, J., Casanova, R. & Barbaux, Y. XPS studies of V<sub>2</sub>O<sub>5</sub>, V<sub>6</sub>O<sub>13</sub>, VO<sub>2</sub> and V<sub>2</sub>O<sub>3</sub>. *Journal of Electron Spectroscopy and Related Phenomena* **71**, 249-261, doi:[https://doi.org/10.1016/0368-2048\(94\)02291-7](https://doi.org/10.1016/0368-2048(94)02291-7) (1995).
- 39 Yang, X. *et al.* Mechanistic Insights into Electrochemical Nitrogen Reduction Reaction on Vanadium Nitride Nanoparticles. *Journal of the American Chemical Society* **140**, 13387-13391, doi:10.1021/jacs.8b08379 (2018).
- 40 Feng, X. *et al.* Three-dimensional nitrogen-doped graphene as an ultrasensitive electrochemical sensor for the detection of dopamine. *Nanoscale* **7**, 2427-2432, doi:10.1039/C4NR06623E (2015).
- 41 Pang, Q. *et al.* A nitrogen and sulfur dual-doped carbon derived from polyrhodanine@cellulose for advanced lithium-sulfur batteries. *Adv Mater* **27**, 6021-6028, doi:10.1002/adma.201502467 (2015).
- 42 Yu, H. *et al.* Adsorption of gold from thiosulfate solutions with chemically modified activated carbon. **36**, 408-428, doi:10.1177/0263617417698864 (2018).
- 43 Masikhwa, T. M. *et al.* Asymmetric supercapacitor based on VS<sub>2</sub> nanosheets and activated carbon materials. *RSC Advances* **6**, 38990-39000, doi:10.1039/C5RA27155J (2016).
- 44 Rao, Y. *et al.* Vanadium sulfides interwoven nanoflowers based on in-situ sulfurization of vanadium oxides octahedron on nickel foam for efficient hydrogen evolution. *Applied Surface Science* **423**, 1090-1096, doi:<https://doi.org/10.1016/j.apsusc.2017.06.218> (2017).
- 45 Zhou, Y. *et al.* Vanadium sulfide sub-microspheres: A new near-infrared-driven photocatalyst. *Journal of Colloid and Interface Science* **498**, 442-448, doi:<https://doi.org/10.1016/j.jcis.2017.03.081> (2017).
- 46 Zhu, L., Li, C., Ren, W., Qin, M. & Xu, L. Multifunctional vanadium nitride@N-doped carbon composites for kinetically enhanced lithium-sulfur batteries. *New Journal of Chemistry* **42**, 5109-5116, doi:10.1039/C8NJ00125A (2018).

- 47 Fan, F. Y., Carter, W. C. & Chiang, Y. M. Mechanism and Kinetics of Li<sub>2</sub>S Precipitation in Lithium-Sulfur Batteries. *Adv Mater* **27**, 5203-5209, doi:10.1002/adma.201501559 (2015).
- 48 Hagen, M. *et al.* In-Situ Raman Investigation of Polysulfide Formation in Li-S Cells. **160**, A1205-A1214, doi:10.1149/2.045308jes (2013).
- 49 McBrayer, J. D., Beechem, T. E., Perdue, B. R., Apblett, C. A. & Garzon, F. H. Polysulfide Speciation in the Bulk Electrolyte of a Lithium Sulfur Battery. **165**, A876-A881, doi:10.1149/2.0441805jes (2018).
- 50 Lei, T. *et al.* Inhibiting Polysulfide Shuttling with a Graphene Composite Separator for Highly Robust Lithium-Sulfur Batteries. *Joule* **2**, 2091-2104, doi:<https://doi.org/10.1016/j.joule.2018.07.022> (2018).
- 51 Nicol, E. A. *et al.* “Surface-enhanced Raman spectroscopy studies of the passive layer formation in gold leaching from thiosulfate solutions in the presence of cupric ion”. **18**, 1469-1484, doi:10.1007/s10008-013-2320-z (2014).
- 52 Jeffrey, M. I., Watling, K., Hope, G. A. & Woods, R. Identification of surface species that inhibit and passivate thiosulfate leaching of gold. *Minerals Engineering* **21**, 443-452, doi:<https://doi.org/10.1016/j.mineng.2008.01.006> (2008).

## Biography of Authors

**Dr. Usman Zubair** secured his PhD in Chemical Engineering in early 2019 from Politecnico di Torino, Italy. He is currently working as postdoc research associate in electrochemistry group at Department of Applied Science and Technology, Politecnico di Torino. His research interests focus on development of novel electrode materials for energy storage devices (i.e.) Li-ion, post lithium ion batteries (Li/S, Li/air) and supercapacitors technologies, and more recently to enquire the involved mechanisms.



**Dr. Julia Amici** has a PhD in Material Sciences and Engineering from Politecnico di Torino (Italy). She conducted her Post Doc in the Electrochemistry Group at Politecnico di Torino DISAT, on post Li-ion technologies, in particular Li-air and Li-Sulfur batteries. She has been involved in the European projects STABLE (Li-Air) and ALISE (Li-Sulfur), and in many national and regional projects on Li-Air and Li-ion systems. She is currently Assistant Professor at PoliTO and her research activities are focused on synthesis and characterization of highly efficient cathode materials as well as polymer electrolytes for Li-ion, Li-air and Li-S batteries.



**Prof. Carlotta Francia** received her Ph.D. degree in material science and technology from Politecnico di Torino followed by research in materials for batteries and electrochemistry. Her research topics are focused on Li-ion, Li-S, metal-air batteries and fuel cells. She is professor of Chemistry at Politecnico di Torino. She participated 5 EU and several national funded projects on batteries, fuel cells and electrochromic devices.



**Prof. Silvia Bodoardo** is associate professor at Politecnico di Torino. Her research activity is mainly focused on the study of materials for Li-ion and post Li-ion batteries, i.e. Li-S, Li-air. She participated in several funded project (coordinator of STABLE project) and several national and regional. She is in the core group of Battery2030+ Large Research Initiative and expert in BatteRIesEurop ETIP. Silvia organized several conferences and workshops on materials with electrochemical application and is author of more than 80 papers on these topics.



## Highlights

- Heterostructured vanadium oxide nitride ( $\text{VO}_x\text{N}_y$ ) nanoparticles in nitrogen doped reduced graphene oxide aerogel has been proposed as host material for sulfur cathode.
- A simple and novel course is opted to realize nitridation and carbonization concurrently.
- A detailed insight of interaction mechanism between  $\text{VO}_x\text{N}_y$  and LiPS is probed through in-operando Raman spectroscopy, XPS and electrochemical methods.
- Lithium polysulfides catalytic conversion is established using  $\text{VO}_x\text{N}_y$  along with stable electrochemical performances.